Journal of Solid State Chemistry 183 (2010) 2726–2730

Contents lists available at ScienceDirect

Journal of Solid State Chemistry

journal homepage: www.elsevier.com/locate/jssc

A simple and general route for the preparation of pure and high crystalline nanosized lanthanide silicates with the structure of apatite at low temperature

Stanislav Ferdov [a,b,c], Protima Rauwel [d], Zhi Lin [a,*], Rute A. Sá Ferreira [b], Augusto Lopes [d]

[a] Department of Chemistry, CICECO, University of Aveiro, 3810-193 Aveiro, Portugal
[b] Department of Physics, CICECO, University of Aveiro, 3810-193 Aveiro, Portugal
[c] Department of Physics, University of Minho, 4800-058 Guimarães, Portugal
[d] Department of Ceramic and Glass Engineering, CICECO, University of Aveiro, 3810-193 Aveiro, Portugal

ARTICLE INFO

Article history:
Received 21 May 2010
Received in revised form
8 September 2010
Accepted 14 September 2010
Available online 18 September 2010

Keywords:
Rare earth silicate
Apatite
Hydrothermal
Nano

ABSTRACT

Rare earth silicates with the structure of apatite are attracting considerable interest since they show oxygen ion conductivities higher than that of yttria-stabilized zirconia (YSZ) at moderate temperature. Based on the hydrothermal synthesis we presented a simple one step process for the direct preparation of the pure and the high crystalline nanosized rare earth silicates with the structure of apatite under a mild condition (230 °C). Since the preparation of the high crystalline silicon based rare earth apatites is performed at high temperature previously and accompanied by subsequent process of grinding, results of this work provide a promising alternative of the existing methodology. Furthermore, due to the relatively low temperature of the preparation of these materials, high doping of monovalent cation can be done, which was not achieved before.

1. Introduction

It is well known that the YSZ is a good oxide ion conductor only at high temperature. However, reduced operating temperature can result in lower costs, a wider choice of cell materials, improved reliability and longer cell life. Within this effort, rare earth silicates with the apatite-type structure attract considerable attention since they show conductivities higher than YSZ at moderate temperature (for example, $\sigma = 1 \times 10^{-3}$ S cm^{-1} for YSZ and 4.3×10^{-3} S cm^{-1} for $La_{10}(SiO_4)_6O_3$ at 500 °C, respectively) and, therefore, are promising candidates for solid oxide fuel cell electrolytes [1–6]. They are also valuable for potential applications as luminescent materials [7–9]. La-based oxyapatite once displayed the highest oxide ion conductivity in the $Ln_{10-x}(SiO_4)_6O_{2\pm y}$ (Ln=rare earth) series [1–5]. Recent experiments on alkaline and alkaline earth doped rare earth oxyapatites showed values of conductivity comparable to that of the $La_{10-x}(SiO_4)_6O_{2\pm y}$ [10,11]. The majority of the syntheses of rare earth silicate apatites are performed at high temperature and the product is often contaminated with impurities [2]. For instance, the ordinary synthesis of La-based oxyapatites is carried out at temperature higher than 1000 °C since well crystallized products are obtained mainly over 1000 °C [11–13]. An alternative to the high temperature synthesis is the mechanical milling of oxides. However, the product from the mechanical milling of oxides is poorly crystallized [14] and often accompanied with non-reacted oxides. A recently presented mild hydrothermal synthesis of europium and mixed europium–gadolinium silicate apatites [9] is a new promising method because it allows low reaction temperature and it can be better controlled from the initial batch to the product, giving highly crystalline and pure apatite silicates. Furthermore, previously reported rare earth silicate apatites need be ground to get fine powders before sintering to achieve dense materials, which is essential for technological aspects, such as solid oxide fuel cell electrolytes [2,10]. To the best of our knowledge no study on the direct preparation of pure and high crystalline oxyapatite nanoparticles at low temperature has been reported. Concerning that the nanometric scale of rare earth silicate apatites will give a solution of the above-mentioned problems and open new potential applications, here we present a simple and general soft chemistry route for one-step preparation of high crystalline rare earth silicates with the structure of apatite. By controlling the synthesis condition we are able to obtain pure and high crystalline nanoparticles of rare earth silicates directly at moderate temperature (230 °C). To prove the generality of the method we reported rare earth silicate apatites containing heavy (Tb^{3+}) and light (La^{3+}) lanthanide ions, respectively.

* Corresponding author.
E-mail address: zlin@ua.pt (Z. Lin).

0022-4596/$ - see front matter © 2010 Elsevier Inc. All rights reserved.
doi:10.1016/j.jssc.2010.09.019

2. Experimental

The hydrothermal synthesis of lanthanide silicates with the apatite-type structure was carried out from a gel with the following chemical composition: 0.4–0.6 Na_2O:0.1–0.2 Ln_2O_3:0.5–0.8 SiO_2:100–200 H_2O. In a typical synthesis, 0.1 g of SiO_2 (silicagel, Merck) was added to a solution with 0.92 g of NaOH (99.9%, Aldrich) in 2.4 g of distilled water. Subsequently, 0.3 g of $TbCl_3 \cdot 6H_2O$ (99.9%, Aldrich) or 0.47 g of $LaCl_3 \cdot 7H_2O$ (99.9%, Aldrich) dissolved in 2.4 g of distilled water was added to the above solution. The mixture was homogenized for 60 min under stirring and then transferred into 45 ml teflon-lined autoclaves. The crystallization was performed under static conditions at 230 °C for 168 h. After fast cooling with flowing water the product was centrifuged, washed with distilled water and dried at 50 °C for one day.

The powder X-ray diffraction (XRD) patterns were collected at room temperature in a step-scan regime (step 0.05 and time 1 s) on a Philips X'Pert MPD diffractometer with Ni-filtered Cu$K\alpha$ X-radiation in the range 2θ 5–50°. The unit cell parameters were refined by the FullProf programme [15]. Energy dispersive X-ray spectrometry (EDS) analyses were carried out by Römteck EDS system attached to the scanning electron microscope (a Hitachi S-4100 microscope). Transmission electron microscopy (TEM) images were recorded on a Hitachi 9000 NA microscope operated at 200 kV. The particle sizes were measured by using dynamic light scattering (DLS) analyses at room temperature with MPT-2 particle size analyzer. Fourier transform infrared spectra (FTIR) of powdered samples suspended in KBr pallets were acquired between 400 and 4000 cm^{-1} using a Mattson Mod 7000 spectrometer.

3. Results and discussions

Fig. 1 shows the calculated (Le Bail fit) [16] and indexed experimental powder XRD patterns of the as-synthesized lanthanum and terbium silicate materials with the structure of apatite. All peaks in the experimental powder XRD patterns can be assigned to a hexagonal symmetry of lanthanide silicate apatites without the indication of any other crystalline by-products, displaying the formation of pure lanthanum and terbium silicates with the structure of apatite. The high intensity and well resolved diffraction peaks indicate the high crystallinity of the samples. The unit cell parameters of both phases were refined [15] assuming hexagonal symmetry and space group $P6_3/m$. Compared with the published data of the lanthanum oxyapatite (PDF-32-1109: $a=b=9.692$, $c=7.182$ Å, $V=584.3$ Å^3), and terbium oxyapatite ($a=b=9.390$, $c=6.840$ Å, $V=522.3$ Å^3) [13], the lattice of the hydrothermally prepared phases (lanthanum $a=b=9.734(1)$, $c=7.155(2)$ Å, $V=587.1(4)$ Å^3; terbium $a=b=9.459(9)$, $c=6.850(7)$ Å, $V=530.9(4)$ Å^3) shows slight extension along a and b axes. When compared the c-axis the lanthanum phase shows shrinkage while the terbium one shows elongation, which could be due to different distribution of Na^+ ions and cationic vacancies between 4f and 6h Wyckoff positions in the apatite structure [9]. The demonstrated mild hydrothermal method is also suitable for the synthesis of other rare earth silicates with the apatite structure (see XRD patterns in Fig. S1 of the Supporting Information). The broadened powder XRD peaks of both apatite samples result from the small crystallite sizes on the nanometer scale. Average crystallite sizes of the synthesized terbium and lanthanum oxyapaites were estimated from the line broadening of (200), (111), (002) peaks in XRD patterns using the Scherrer formula [17] $L=k\lambda/\beta \cos\theta$, where L is the crystallite size, k is the Scherrer constant usually taken as 0.89, λ is the wavelength of X-ray radiation (1.5418 Å for Cu$K\alpha$), and β is the full-width at half-maximum (fwhm) of diffraction peak

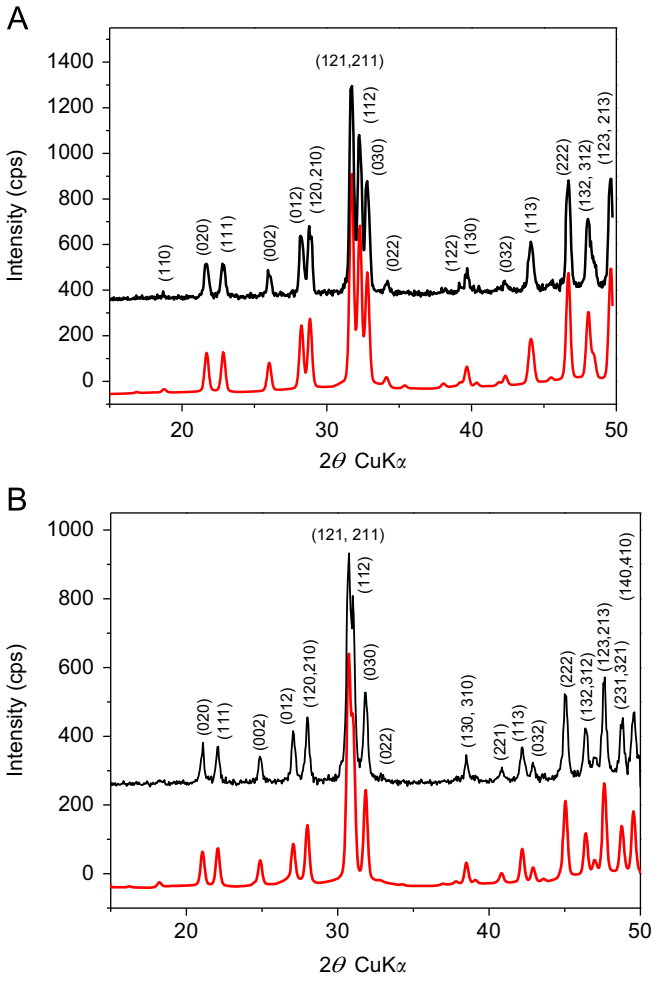

Fig. 1. Calculated (below) and experimental powder XRD patterns of terbium (A) and lanthanum (B) apatites.

measured at 2θ. The calculations gave a crystallite size about 71 nm for the terbium sample, which is compatible with the particle size obtained from TEM images. In contrast to the terbium phase, the powder XRD pattern of the lanthanum sample shows slightly sharper reflections, which gave the crystallite sizes of about 84 nm.

In order to make sure that the individual particles are well crystallized, the transmission electron microscopy (TEM) images were recorded. Fig. 2a shows a TEM image of an assembly of the terbium apatite powder, which contains almost spheroidal nanoparticles of 15–40 nm. This is compatible with the calculated values using Scherrer formula from the powder XRD data. The inset of this image shows the selected area electron diffraction (SAED) pattern of the same assembly of particles. The brightest rings correspond to the (100), (110) and (211) reflections from the apatite structure of the terbium silicate obtained from simulations, showing the polycrystalline characteristic of the aggregate. Furthermore, Fig. 2b shows the high resolution transmission electron micrograph of one terbium silicate apatite crystallite, confirming its mono crystalline characteristic. The inset in the top left hand corner is the fast Fourier transform (FFT) of the particle with (002) reflections corresponding to the 110 zone axis. The second inset in the figure is the FFT filtered image of the zone and gives a lattice spacing of 0.68 nm, which corresponds to the c lattice parameter of the terbium silicate apatite structure.

The TEM results of lanthanum silicate apatite in Fig. 3 are similar to that of terbium silicate apatite, also confirming its

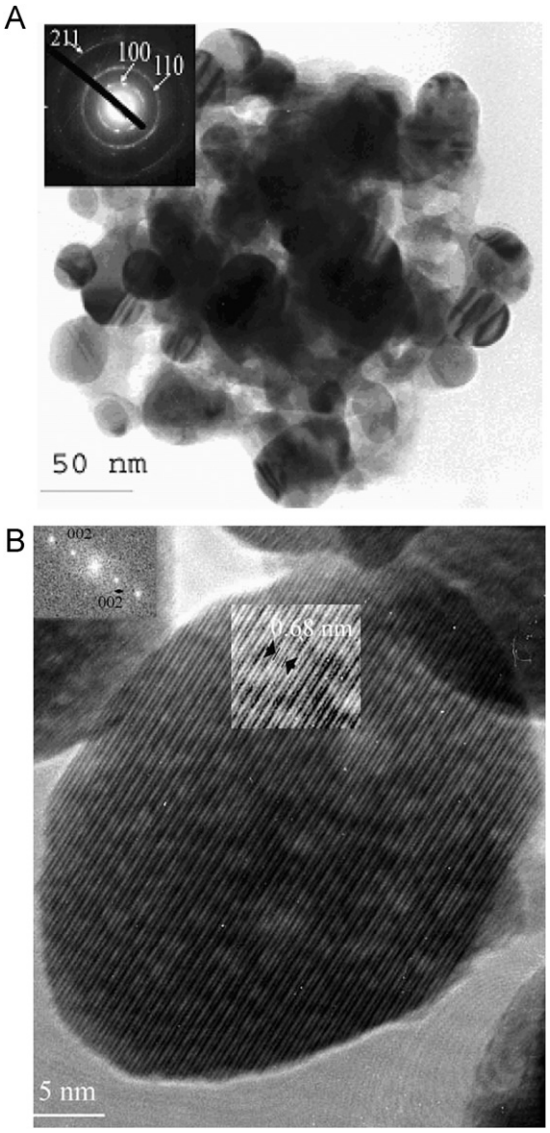

Fig. 2. Bright field image of an assembly of Tb silicate apatite particles with the inset showing it's SAED pattern (A) and a high resolution image of a Tb silicate apatite particle, the top left hand inset is a FFT of the particle and the second inset is the FFT filtered image of the zone (B).

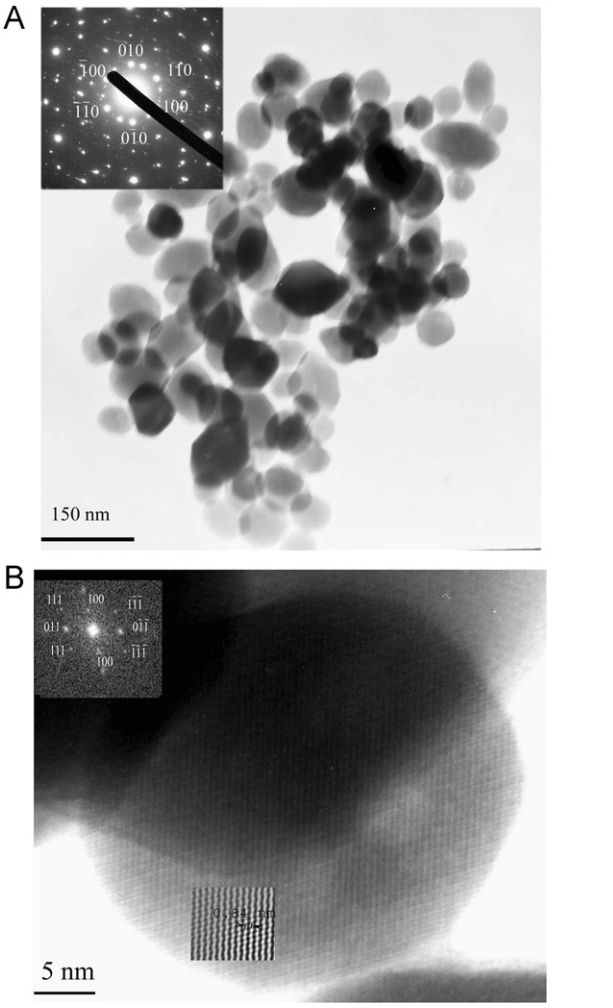

Fig. 3. Bright field image of an assembly of La silicate apatite particles with the inset showing it's SAED pattern (A) and a high resolution image of a La silicate apatite particle, the top left hand inset is a FFT of the particle and the second inset is the FFT filtered image of the zone (B).

mono crystalline characteristic. Fig. 3a shows a TEM image of an assembly of lanthanum silicate apatite nanoparticles of 30–100 nm. This result deviates from the calculated particle size from the powder XRD data using Scherrer formula, which may be due to the less spherical shape when comparing with the terbium phase. The inset of this image is the SAED pattern and shows a preferential orientation of a larger number of particles. The reflections correspond to the *c*-axis orientation. Fig. 3b is the high resolution micrograph and shows the mono crystalline nature of lanthanum silicate apatite particles. The inset in the left hand corner corresponds to the FFT for this particle, giving a $0\bar{1}1$ zone axis. The second inset in this figure is the FFT filtered image and the (100) plane spacing was calculated to be 0.84 nm which was used to calculate $a=b=0.97$ nm.

From TEM images, particle size distribution histograms were used to measure the average particle size using a Gaussian fit. Even though there was an obvious overlap of the particles (Figs. 2a and 3a), many particles appear distinct and therefore are measurably by TEM. The particle size histogram contains not only the particles in Figs. 2a and 3a but also from other micrographs (not shown here). Average particle sizes thus obtained were estimated to be 19 nm for the Tb and 38 nm for the La apatites, respectively (Fig. S2 in the Supporting Information). The discrepancy of particle sizes obtained from XRD and TEM may be because that Scherrer formula is not accurate for non-spherical particles and that a few relative large particles will cause a significant decrease of XRD line width. The particle size distribution of the synthesized lanthanide silicate apatites was also studied by DLS measurement. The measured mean hydrodynamic radii are 370 and 431 nm for the terbium and lanthanum phases, respectively (Fig. S3 in the Supporting Information), which are actually the size of the observed particle assemblies (see TEM images). The presence of only one distribution peak indicates that all particles in terbium and lanthanum silicate apatites are included in aggregates with similar size.

EDS analysis gives *M*/Si ratio of 1.92 and 2.27 (M=La, Tb and Na) for lanthanum and terbium samples, respectively. This ratio is higher than the ideal one (1.67), which may result from the combination of the different effects. When monovalent cation (Na^+) substitutes a trivalent one (La^{3+}, Tb^{3+}), anionic vacancies may be created or the number of OH^- ions may increase at the expense of O^{2-} ions in order to keep the charge balance [9]. On the other hand, Tolchard et al. [18] studied the solution energies of a wide range of M^+, M^{2+}, M^{3+} and M^{4+} dopants on Si and La positions in

$La_{9.33}Si_6O_{26}$ using computer modeling techniques and showed that an unusually broad range of dopant ions (with the different size and charge state) can substitute for La in the $La_{9.33}Si_6O_{26}$ apatite, being in accord with current experimental data. Their results for M^+ showed a clear preference for monovalent dopants (e.g., Na, K) to substitute into the La site and with compensation from incorporation of additional cations as the interstitial defects. When they considered oxygen vacancy, the results showed relative high energies. EDS analysis gives M/Na ratio of 1.95 ($\pm$0.3) and 1.08 ($\pm$0.1) (M=La and Tb) for lanthanum and terbium samples, respectively. Based on their results, the M/Si ratios of our samples may be 1.48 and 1.54, which give M:Si=8.86:6 and 9.24:6 for lanthanum and terbium apatites, respectively. These ratios are reasonable for *Ln* apatites. In fact, only few experiments tested the monovalent doping in the silicate-based apatite materials, largely because of the volatilization of dopant source at the high synthesis temperatures [18] and the content of monovalent doping in the silicate-based apatite materials is relatively low. Our experimental results provided a unique route to prepare rare earth silicate apatite with high monovalent doping, showed the high structural flexibility of the rare earth silicate apatite for high monovalent doping, and the doping behavior for high monovalent doping is still in accord with Tolchard's theoretical calculation. Furthermore, we also cannot rule out other effects on the M/Si ratios. When a particle becomes smaller and smaller, the surface to volume ratio of the particle is increased dramatically. The chemical composition of surface is usually not exactly the same as the bulk. The additional cations of the interstitial defects could also be protons. These also change the total M/Si ratio.

In order to get further proof of the apatite structure, FTIR spectra were recorded and Fig. 4 shows the spectra of lanthanum and terbium samples which are very similar to that of previously reported rare earth silicate apatite materials [9,19]. The spectrum of lanthanum sample exhibits bands at: 975, 915, 543, 494 cm^{-1} and shoulder at about 880 cm^{-1}, and all of them can be assigned to the lanthanum silicate apatite [19]. The spectrum of terbium sample exhibits bands at: 978, 935, 562, 501 cm^{-1} and shoulder at about 880 cm^{-1}, which is very similar to that of europium silicate apatite [9]. The bands and shoulder at 975, 915, 880 cm^{-1} for lanthanum sample and 975, 935, 880 cm^{-1} for terbium sample, respectively, belong to asymmetric stretching modes of SiO_4 group [19]. The bands at 543, 494 cm^{-1} for lanthanum sample and 562, 501 cm^{-1} for terbium sample, respectively, result from asymmetric bending modes of SiO_4 group [19] and *Ln*–O vibration modes [20].

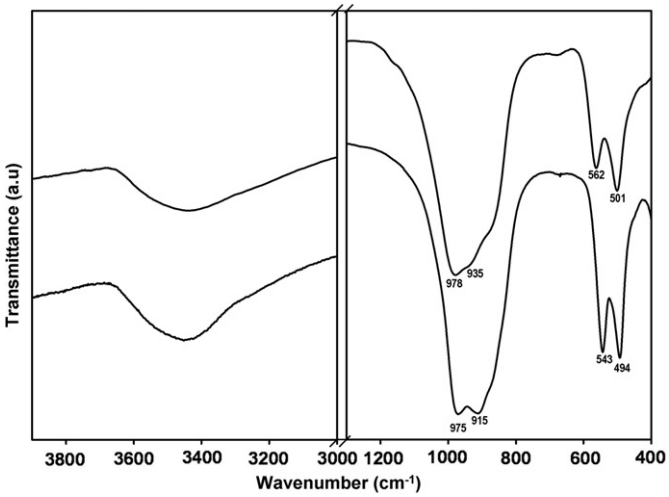

Fig. 4. FTIR spectra of lanthanum (bottom) and terbium (top) silicates with the structure of apatite.

The broadband between 3300 and 3660 cm^{-1} arises from the O–H bond stretching modes and indicates a presence of hydrous species. Same as those of Eu and Eu–Tb apatites [9] no any sharp peak was found in this region. As already discussed in our previous work [9], low OH content is expected.

Tolchard et al. [21] also studied the mechanistic features of oxygen ion transport in the $La_{9.33}Si_6O_{26}$ and $La_8Sr_2Si_6O_{26}$ apatites at the atomic level using computer modeling techniques and predicted a position of the interstitial oxygen in these materials. The predicted position has been determined later by neutron powder diffraction data [22]. Tolchard's calculation [21] showed that interstitial oxygen migrates in a sinusoidal-like pathway along *c*-axis for $La_{9.33}Si_6O_{26}$ while the Sr doping changes the mechanism of the oxygen ion conductivity. The neutron powder diffraction [22] showed that the oxygen ion conductivity is controlled by the lanthanum vacancies at certain position, the interstitial oxygen and the oxygen vacancies in the lanthanum surrounded channel. It is clear that high monovalent doping will affect those characteristics which control the oxygen ion conductivity. The materials obtained from this process may be used to study the effect of high monovalent doping content on the oxygen ion conductivity. It is most likely that at high monovalent doping, the high content of extra cations will decrease lanthanum and oxygen vacancies, and interstitial oxygen, therefore, decrease the oxygen ion conductivity. It is interesting to prepare samples with low monovalent doping content in future to improve the pure oxygen ion conductivity. Finally, since the materials obtained from this process contain both cation and anion as charge carriers, they may have other interesting properties.

4. Conclusions

In summary, pure and high crystalline nanosized rare earth silicates with the apatite-type structure can be prepared under the mild hydrothermal condition (230 °C). The powder XRD and TEM studies proved that the samples had nanosize, pure apatite structure, and with high crystallinity. EDS analysis suggested a high monovalent doping. The results of this work provide a much better alternative of the existing methodology for the synthesis of rare earth silicate apatite materials and provide a route to prepare rare earth silicate apatite with high monovalent doping. Furthermore, the nano powder has high surface area and is usually more active for sintering. The high crystalline nano powder gives new opportunity to obtain highly dense green pallet and to sinter pallets at lower temperature, which may modify the performance of the materials.

Acknowledgment

This work was supported by FCT, POCI2010, PTDC, FSE, and FEDER. S. Ferdov is on leave from the Central Laboratory of Mineralogy and Crystallography, Bulgarian Academy of Sciences.

Appendix A. Supporting Information

Supplementary data associated with this article can be found in the online version at doi:10.1016/j.jssc.2010.09.019.

References

[1] Y. Higuchi, M. Sugawara, K. Hawazaki, K. Uewatsu, S. Nakayama, Patent 2004/0161651 A1.
[2] S. Nakayama, M. Sakamoto, J. Eur. Ceram. Soc. 18 (1998) 1413.
[3] H. Arikawa, H. Nishiguchi, T. Ishihara, Y. Takita, Solid State Ionics 136 (2000) 31.

[4] S. Nakayama, T. Kageyama, H. Aono, Y. Sadaoka, J. Mater. Chem. 5 (1995) 1801.
[5] M.S. Islam, J.R. Tolchard, P.R. Slater, Chem. Commun. (2003) 1486.
[6] T. White, C. Ferraris, J. Kim, S. Madhavi, Rev. Mineral. Geochem. 75 (2005) 307.
[7] G. Blasse, Mater. Chem. Phys. 16 (1987) 201.
[8] M. Tachihante, D. Zambon, J.C. Cousseins, Eur. J. Solid State Inorg. Chem. 33 (1996) 713.
[9] S. Ferdov, R.A. Sá Ferreira, Z. Lin, Chem. Mater. 18 (2006) 5958.
[10] P.R. Slater, J.E.H. Sansom, J.R. Tolchard, Chem. Rec. 4 (2004) 373.
[11] V. Maisonneuve, E. Leduc, O. Bohnke, M. Leblanc, Chem. Mater. 16 (2004) 5220.
[12] S. Tao, J.T.S. Irvine, Mater. Res. Bull. 36 (2001) 1245.
[13] J. Felsche, J. Solid State Chem. 5 (1972) 266.
[14] A.F. Fuentes, E. Rodríguez-Reyna, L.G. Martínez-González, M. Maczka, J. Hanuza, U. Amador, Solid State Ionics 177 (2006) 1869.
[15] J. Rodriguez-Carvajal, Fullprof 2k, version 3.4, November 2005; Laboratoire Leon Brillouin (CEA/CNRS), CEA-Saclay, Gif-sur-Yvette Cedex, France.
[16] A. Le Bail, H. Duroy, J.L. Fourquet, Mater. Res. Bull. 23 (1988) 447.
[17] H.P. Klug, L.E. Alexander, X-ray Diffraction Procedure, 2nd ed., Wiley New York, 1974 (Chapter 9).
[18] J.R. Tolchard, P.R. Slater, M.S. Islam, Adv. Funct. Mater. 17 (2007) 2564.
[19] E. Rodríguez-Reyna, A.F. Fuentes, M. Maczka, J. Hanuza, K. Boulahya, U. Amador, J. Solid State Chem. 179 (2006) 495.
[20] R. Kannan, S. Mohan, Mater. Sci. Eng. B86 (2001) 113.
[21] J.R. Tolchard, M.S. Islam, P.R. Slater, J. Mater. Chem. 13 (2003) 1956.
[22] L. León-Reina, E.R. Losilla, M. Martínez-Lara, S. Bruque, M.A.G. Aranda, J. Mater. Chem. 14 (2004) 1142.